



1 **Current potential of CH₄ emission estimates using TROPOMI in the Middle East**

2

3 Mengyao Liu^{1*}, Ronald van der A¹, Michiel van Weele¹, Lotte Bryan^{1,2}, Henk Eskes¹,
4 Pepijn Veefkind^{1,2}, Yongxue Liu³, Xiaojuan Lin^{1,4}, Jos de Laat¹, Jieying Ding¹

5 ¹ KNMI, Royal Netherlands Meteorological Institute, De Bilt, The Netherlands

6 ² Delft University of Technology, Delft, The Netherlands

7 ³ School of Geographic and Oceanographic Sciences, Nanjing University, Nanjing,

8 China

9 ⁴ Department of Earth System Science, Ministry of Education Key Laboratory for Earth
10 System Modeling, Tsinghua University, Beijing, China

11 * Correspondence to: Mengyao Liu (mengyao.liu@knmi.nl)

12 **Abstract**

13 An improved divergence method has been developed to estimate annual methane (CH₄)
14 emissions from TROPospheric Monitoring Instrument (TROPOMI) observations. It
15 has been applied to the period of 2018 to 2021 over the Middle East, where the
16 orography is complicated, and the mean mixing ratio of methane (XCH₄) might be
17 affected by albedos or aerosols over some locations. To adapt to extreme changes of
18 terrain over mountains or coasts, winds are used with their divergent part removed. A
19 temporal filter is introduced to identify highly variable emissions and further exclude
20 fake sources caused by retrieval artifacts. We compare our results to widely used
21 bottom-up anthropogenic emission inventories: Emissions Database for Global
22 Atmospheric Research (EDGAR), Community Emissions Data System (CEDS) and
23 Global Fuel Exploitation Inventory (GFEI) over several regions representing various
24 types of sources. The NO_x emissions from EDGAR and Daily Emissions Constrained
25 by Satellite Observations (DECSO), and the industrial heat sources identified by Visible
26 Infrared Imaging Radiometer Suite (VIIRS) are further used to better understand our
27 resulting methane emissions. Our results indicate possibly large underestimations of
28 methane emissions in metropolises like Tehran (up to 50%) and Isfahan (up to 70%) in
29 Iran. The derived annual methane emissions from oil/gas production near the Caspian
30 Sea in Turkmenistan are comparable to GFEI but more than two times higher than
31 EDGAR and CEDS in 2019. Large discrepancies of distribution of methane sources in
32 Riyadh and its surrounding areas are found between EDGAR, CEDS, GFEI and our



33 emissions. The methane emission from oil/gas production in the east to Riyadh seems
34 to be largely overestimated by EDGAR and CEDS, while our estimates, and also GFEI
35 and DECISO NO_x indicate much lower emissions from industry activities. On the other
36 hand, regions like Iran, Iraq, and Oman are dominated by sources from oil and gas
37 exploitation that probably includes more irregular releases of methane, with the result
38 that our estimates, that include only invariable sources, are lower than the bottom-up
39 emission inventories.



40 **1 Introduction**

41 Methane (CH₄) is the second most important greenhouse gas of which the abundance
42 kept increasing in the last decades (Turner et al., 2019; Saunio et al., 2020; Eyring et
43 al., 2021), with a short-term stable concentration level between the years 2000 and 2006
44 (Dlugokencky et al., 2009; Rigby et al., 2008). The relatively short lifetime of about a
45 decade makes CH₄ emissions a short-term target for mitigating climate change. The
46 TROPOspheric Monitoring Instrument (TROPOMI) on board the Sentinel 5 Precursor
47 (S5-P) satellite provides an opportunity to measure CH₄ globally at a high resolution of
48 7×7 km² since its launch in October 2017 (upgraded to 5.5×7 km² in August 2019)
49 (Veefkind et al., 2012; Lorente et al., 2021). Previous studies have demonstrated the
50 capability of TROPOMI to identify big CH₄ emitters (e.g., leakages from pipelines)
51 through detecting large anomalies or to derive regional emission fields (de Gouw et al.,
52 2020; Pandey et al., 2019; Zhang et al., 2020; Chen et al., 2023).

53 However, using observations from TROPOMI to quantify emissions are also facing
54 challenges. On the one hand, some sources are located near the coast or in places with
55 complex topography, where satellite observations are often of reduced quality. The
56 observations of TROPOMI CH₄ contain uncertainties from retrieval assumptions for
57 surface albedo, aerosols, and the sun-glint model over the ocean. On the other hand, the
58 characteristics of the various sources are poorly understood. For instance, constant
59 emitting sources from landfills *versus* intermittent leakage of oil/gas, makes it difficult
60 to quantify their emissions (Varon, 2021).

61 The Middle East is one of the strong CH₄-emitting regions in the world (Chen et al.,
62 2023). Nevertheless, these emissions are particularly challenging to be quantified
63 because of the aspects aforementioned. Lauvaux et al. (2022) found fewer detections
64 of ultra-emitters (>25 kg/hour) in Middle Eastern countries like Iraq, Saudi Arabia than
65 other hot-spot regions like the U.S. from TROPOMI observations. Chen et al., (2023)
66 also revealed large discrepancies between a priori and posterior emission inventory
67 derived from satellites over the Middle East.

68 In this study, we present an improved divergence method (Beirle et al., 2019; Liu et al.,
69 2021; Veefkind., 2023) to quantify the emissions of CH₄ over the Middle East from
70 2018 to 2021 on a grid of 0.2° from TROPOMI retrieved XCH₄ by using the latest
71 version of the scientific retrieval product (TROPOMI/WFMD v1.8) from the
72 University of Bremen (Schneising et al., 2023). This inversion algorithm is based on
73 the mass balance theory and is unique because of its speed and no need for a priori
74 knowledge of the sources. The wind divergence was first removed from the daily wind
75 fields to better adapt to the complicated orography in the Middle East, and a temporal
76 filter was developed in this study to exclude incorrect sources caused by retrieval issues,
77 respectively. For an area without influence from retrieval issues (e.g., albedo), the
78 persistence of sources can be further tested by the temporal filter.



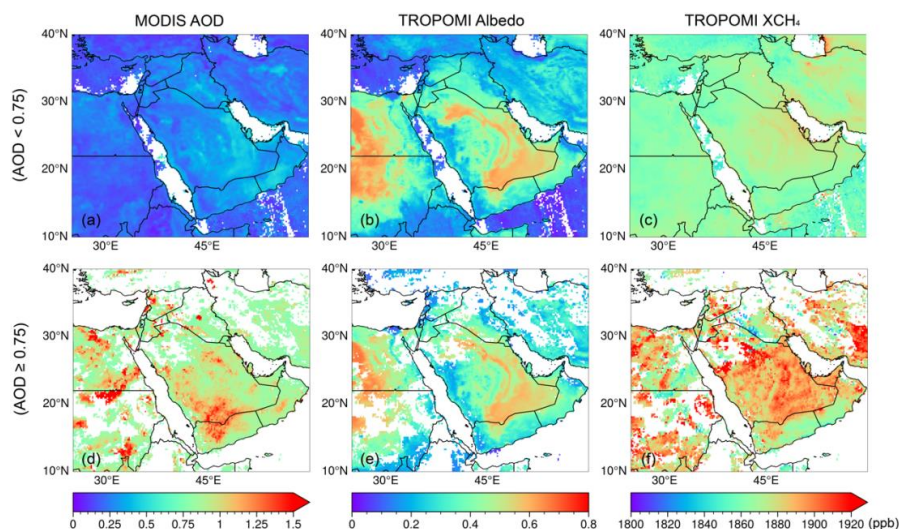
79 Before calculating the divergence, we exclude contaminated pixels with a high aerosol
80 optical depth (AOD) using daily MODIS AOD observations and the global hourly
81 Atmospheric Composition Reanalysis 4 (EAC4) dataset. To a grid cell that shows a
82 strong spatial correlation between the divergence and its corresponding background
83 divergence, a posterior correction is applied to remove the contribution from the
84 inhomogeneous background. The final results are further compared to the total
85 anthropogenic CH₄ emissions from Emissions Database for Global Atmospheric
86 Research (EDGAR) v7.0 (Crippa et al., 2022) and CEDS v_2021_04_21 (O'Rourke et
87 al., 2021). Other auxiliary datasets, such as the methane emissions from the fuel
88 exploitation predicted by GEFI v2 (Scarpelli et al., 2019) and total anthropogenic NO_x
89 emissions from EDGAR v6.1 and DECSO v6.2 (van der A et al., 2024; Ding et al.,
90 2020; Mijling and van der A, 2012) are used for a better interpretation of our results.

91 **2 Data and Methodology**

92 *2.1 Selection of reliable TROPOMI XCH₄ data*

93 This study used the latest TROPOMI WFM-DOAS (TROPOMI/WFMD v1.8) XCH₄
94 product (Schneising et al., 2023). Quality filters were applied to reduce the size of a
95 daily XCH₄ file before making it available to the public. Thus, the daily files contain
96 only the pixels that had passed the quality check. In version 1.8, a de-stripping filter has
97 been applied to each orbit.

98 The TROPOMI/WFMD algorithm has been designed for clear-sky scenes with minor
99 scattering by aerosols and optically thin clouds (i.e., cirrus). Still, a few pixels could
100 contain high aerosol loadings (MODIS AOD at 550 nm ≥ 0.75 , Fig. 1. d–f v.s. a–c),
101 leading to biased high XCH₄. We here use the daily observation of 10 km MODIS/Aqua
102 AOD data at 550 nm, which has a similar overpass time as TROPOMI, to estimate the
103 AOD values for pixels of TROPOMI. The pixels with AOD ≥ 0.75 are filtered, and 1.7%
104 of pixels in 2019 are excluded with this criterion in the domain of 10–40N°, 20–50E°.
105 Admittedly, not every TROPOMI pixel has a collocated MODIS AOD observation.
106 Thus, we used the global hourly EAC4 dataset combined with MODIS daily
107 observations to ensure every pixel of TROPOMI has an AOD estimate to reduce the
108 systematic biases caused by high aerosol loadings while maintaining as many pixels as
109 possible. The details about obtaining an AOD value for each pixel can be found in Part
110 A of the Supplementary Information (SI).



111

112 **Figure 1.** Annual mean of (a) MODIS AOD, (b) albedo in TROPOMI XCH4 retrieval
 113 and (c) TROPOMI XCH4 on a grid of 0.2° in 2019, which are the average of pixels
 114 with AOD < 0.75. (d)-(f) are similar to (a)-(c) but based on the pixels with AOD ≥ 0.75.
 115 Only pixels with available MODIS AOD are used to generate the maps shown here.

116 *2.2 Methane bottom-up emission inventories and auxiliary emission datasets*

117 In this study, EDGAR v7.0 is mainly used to evaluate the result of the derived methane
 118 emissions because it covers the whole period of our study. EDGARv7.0 provides
 119 estimates for emissions of the three main greenhouse gases (CO₂, CH₄, N₂O) per sector
 120 and country from 1970 to 2021 on a grid of 0.1°. The activity data for non-CO₂
 121 emissions are primarily based on the World Energy Balances data (2021) of the IEA.
 122 The activity data for certain sectors are further modified by other updated datasets. For
 123 example, International Fertiliser Association (IFA) and Gas Flaring Reduction
 124 Partnership (GGFR)/U.S. National Oceanic and Atmospheric Administration (NOAA),
 125 United Nations Framework Convention on Climate Change (UNFCCC) and World
 126 Steel Association (worldsteel) recent statistics are used for activity data of energy-
 127 related sectors, and agricultural sectors are further modified by FAO (2021). In addition,
 128 the latest version (v_2021_04_21) of CEDS and the Global Fuel Exploitation Inventory
 129 (GFEI v2) are also used for comparisons in specific years. CEDS v_2021_04_21
 130 consists of CMIP6 historical anthropogenic emissions data from 1980 - 2019 on a grid
 131 of 0.5°. The 0.5° data was further downscaled to 0.1° using 0.1° proxy data from
 132 EDGAR v5.0 emission grids (O'Rourke et al., 2021). GFEI v2 allocates methane
 133 emissions from oil, gas, and coal to a grid of 0.1° by using the national emissions
 134 reported by individual countries to UNFCCC and assign them to infrastructure



135 locations. GFEI v2 inventory is available for 2019 and presents an update of GFEI v1
136 which was made for 2016 (Scarpelli, et al., 2021).

137 Despite that the three above-mentioned inventories have assembled various information
138 from recent statistics, emissions in the Middle East are still uncertain and show large
139 discrepancies because of the lack of reports from the industrial facilities. In addition,
140 NO_x emissions and gas flaring data are often used to analyze the emission of methane,
141 especially for the energy-related sources. Thus, we further used NO_x emissions and
142 industrial heat sources identified by VIIRS (Liu et al., 2018) to better understand the
143 derived methane emissions. The latest NO_x emissions from EDGAR (v6.1, the most
144 recent year is 2018) and the top-down NO_x emission inventory from TROPOMI,
145 DECSO (van der A et al., 2023; Ding et al., 2020), are used to access uncertainties of
146 various emission inventories. For clarity, we combined the source sectors of methane
147 in EDGAR and CEDS, and the sectors of NO_x in EDGAR into two categories: energy
148 and others. The sectors for each category are listed in Table-1.

149



Table 1. Sectors of CH₄ and NO_x used in this study based on EDGAR

Sector Species	Energy	Others
¹ EDGAR v7.0 CH ₄	1, Power industry (1A1a) 2, Refineries and transformation industry (1A1b+1A1ci+1A1cii+1A5biii+1B1b+1B2aiii6+1B2biii3+1B1c) 3, Combustion for manufacturing (1A2) 4, Fuel exploitation (1B1a+1B2aiii2+1B2aiii3+1B2bi+1B2bi i) 5, Chemistry process (2B) 6, Energy for building (1A4 +1A5) 7, Iron and steel production (2C2) 8, Fossil fuel fires (5B)	Transportation 1, Aviation (1A3a) 2, Railways, pipelines, off-road transport (1A3c+1A3e) 3, Shipping (1A3d) Agricultural 1, Manure management (3A2) 2, Agricultural soils (3C2+3C3+3C4+3C7) 3, Enteric fermentation (3A1) Waste 1, Agricultural waste burning (3C1b) 2, Solid waste incineration (4C) 3, Solid waste landfills (4A+4B)
² CEDS v_2021_04_21 CH ₄	1, Energy 2, Industrial 3, Solvents production and application	0, Agriculture 1, Transportation 2, Residential, commercial, other 6, Waste 7, International shipping
EDGAR v6.1 NO _x	1, Power industry (1A1a) 2, Refineries and transformation industry (1A1b+1A1ci+1A1cii+1A5biii+1B1b+1B2aiii6+1B2biii3+1B1c) 3, Combustion for manufacturing (1A2) 4, Fuel exploitation (1B1a+1B2aiii2+1B2aiii3+1B2bi+1B2bi i) 5, Chemistry process (2B) 6, Energy for building (1A4 +1A5) 7, Iron and steel production (2C2) 8, Fossil fuel fires (5B) 9, Non-ferrous metals production (2C3-C5) 10, Food and paper (2H)	Transportation 1, Aviation (1A3a) 2, Railways, pipelines, off-road transport (1A3c+1A3e) 3, Shipping (1A3d) Agricultural 1, Manure management (3A2) 2, Agricultural soils (3C2+3C3+3C4+3C7) Waste 1, Agricultural waste burning (3C1b) 2, Solid waste incineration (4C)

150 ¹The codes in parentheses are based on IPCC 2006 used by EDGAR v7.0 to generate each sector.

151 ²CEDS provides monthly sectoral methane emissions, in which the category is illustrated by the number.

152



153 *2.3 Divergence calculation*

154 The basic methodology has been described in Liu et al. (2021). Here, we have improved
155 the procedure to estimate CH₄ emissions from TROPOMI retrieved XCH₄ consisting
156 of three steps: (1) The use of daily MODIS/Aqua AOD 10 km L2 dataset (v6.1) and
157 daily CAMS gridded AOD re-analysis data to filter unreliable retrievals of TROPOMI
158 XCH₄. (2) Derive the enhancements of XCH₄ in the PBL (XCH₄^{PBL}) and non-divergent
159 winds from ERA5 wind dataset, which are then used to calculate the spatial divergence
160 and the preliminary methane emission. (3) Apply a posterior spatial correction to
161 subtract the contribution of the residue of the regional background, and identify
162 possible false sources by using a temporal filter.

163 Our method to estimate the preliminary methane emission E' over a certain period is
164 based on the divergence method described by Beirle et al. (2019) for NO_x emissions
165 and specifically for methane by Liu et al. (2021):

166
$$E' = \overline{D_d^S} = \overline{\nabla \cdot (X_d^{PBL} - X_d^B) \times A_d^{PBL} \overline{\vec{w}}} \quad (1)$$

167 where D_d^S is the daily divergence of a source. X_d^{PBL} is the daily XCH₄ in the Planetary
168 Boundary Layer (PBL) that is calculated by subtracting the vertical column of methane
169 above the PBL from the TROPOMI observations. This vertical column above the PBL,
170 is based on the model results of EAC4 of CAMS (Inness et al., 2019). This EAC4
171 model run contains no *a priori* CH₄ emissions, which means the daily spatial
172 distribution of methane is only driven by transport in the upper atmosphere, unaffected
173 by sources at the surface. The total dry air column from the EAC4 dataset is constrained
174 by the TROPOMI retrieval for each pixel. We fixed the PBLH at 500 meters above the
175 ground considering the PBLH from the reanalysis dataset has large uncertainties and is
176 occasionally too shallow (Guo et al., 2021). X_d^B is the regional background of X_d^{PBL} ,
177 which is defined as the average of the lower 10 percentile of its surrounding ± 3 grid
178 cells in the zonal direction and meridional direction ($7 \times 7 = 49$ grid cells in total by
179 taking the current grid cell as the center) considering the extensive variations of the
180 orography in the Middle East. The daily regional background is built when more than
181 10 grid cells have valid retrievals in this domain. A_d^{PBL} is the corresponding air density
182 column in the PBL. The details to derive X_d^{PBL} and A_d^{PBL} can be found in Liu et al.
183 (2021). The advantages of including X_d^B are (1) it can be used to diagnose the
184 contribution of inhomogeneous background, especially over mountains and coastal
185 regions, and (2) the system biases between CAMS and TROPOMI, which leads to
186 biased X_d^{PBL} , is included in both and can be greatly reduced by subtracting X_d^B from
187 X_d^{PBL} .

188 The daily wind field ($\overline{\vec{w}}$) halfway the height of the PBL (PBLH) close to the overpass
189 time is obtained from the ECMWF. Wind speeds are constrained between 0 m/s to 10



190 m/s because the divergence method works when advective transport takes place, and
191 extremely high wind speed are unfavorable for a method based on the regional mass
192 balance. Local wind-field changes induced by complicated orography inevitably leads
193 to a certain pattern of wind divergence ($\overline{D_d^W}$), which further influence

$$194 \quad D_d^S = \overline{w} \nabla(XCH_4^{PBL} - XCH_4^B) + (XCH_4^{PBL} - XCH_4^B) \nabla \overline{w} \quad (2)$$

195 Liu et al. (2021) corrected E' by using an empirical correction by using a spatial
196 correlation between $\overline{D_d^S}$ and $\overline{D_d^B}$ to account for the effect of inhomogeneous background
197 and $\nabla \overline{w}$ over Texas, where the terrain is relatively flat and less affected by mountains.
198 To better reduce the effect of winds, we followed the method imposed by Sims (2018)
199 to iteratively remove the gradients of $\nabla \overline{w}$ on each day to get a non-divergent wind field,
200 V component (south-north) and U component (west-east), for the calculation of Eq. (1).

201 The positive values of $\overline{D_d^S}$ due to orography-raised wind near Tehran in Fig. 2d are
202 largely reduced (Fig. 2f) by using a non-divergent wind field. The magnitudes of $\overline{D_d^B}$ in
203 Fig. 2e also get close to $\overline{D_d^S}$. The procedure of removing the wind divergence from the
204 original wind field is explained in Part B in SI.

205 *2.3 Estimating emissions based on the divergence*

206 The inhomogeneous spatial distribution of $\overline{D_d^B}$ indicates the possible residue of the
207 regional background we built in Sect. 2.2. Therefore, we evaluate the contribution from
208 the residue background for each grid cell with positive E' by checking the spatial
209 correlation between $\overline{D_d^B}$ and $\overline{D_d^S}$ in the domain that we defined to build the regional
210 background (its surrounding ± 3 grid cell). For grid cells with positive E' , a linear
211 regression is applied to its surrounding ± 3 cells:

$$212 \quad y_i = k \cdot x_i + b \quad (3)$$

213 where y_i stands for $\overline{D_d^S}$ and x_i stands for $\overline{D_d^B}$ of grid i . k and b are the slope and intercept
214 of the linear regression, respectively. If Eq. (3) is applicable to the center grid, it implies
215 the residue of the background still contributes to E' and should be subtracted. This
216 linear correlation can be distinctive over locations with large variations in orography
217 (e.g., mountains, coastal areas). If more than 68% of the grid cells and the grid cell itself

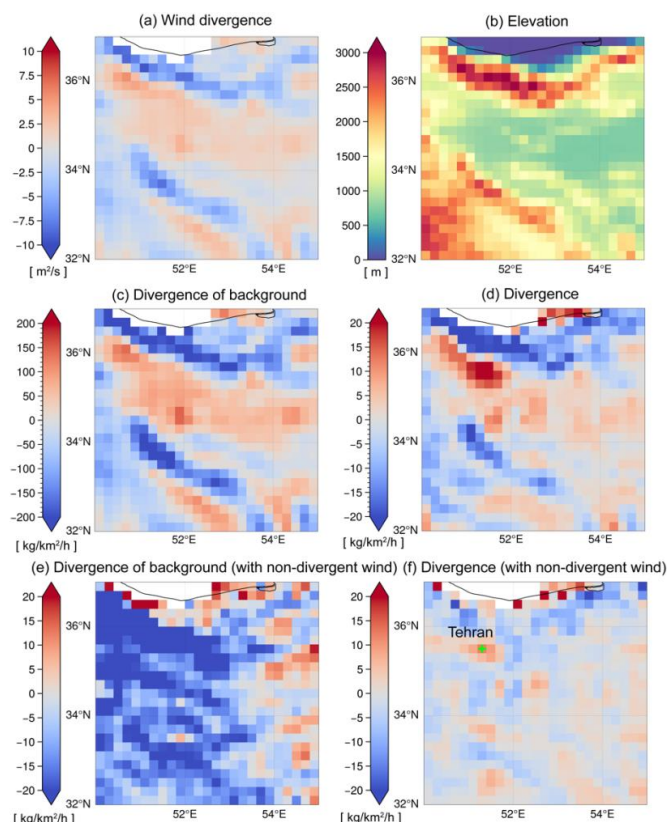


218 fall within the prediction lines of Eq. (3), estimated emissions are set to zero because
219 \overline{D}_d^S can be fully predicted by \overline{D}_d^B according to Eq. (3). The grid cells are considered to
220 be influenced by residue background only when Eq. (3) is significant (p-value < 0.01),
221 and they are further corrected by the spatial correction:

$$222 \quad E^{corr} = E' - (k \cdot \overline{D}_d^B + b) \quad (4)$$

223 in which $(k \cdot \overline{D}_d^B + b)$ is regarded as the contribution from the remaining background,
224 which should be subtracted from the preliminary estimated emissions, E' . In addition,
225 we find that areas with negative E' together with negative \overline{D}_d^B , implying no significant
226 sources exist. The final estimated emissions at grid cells with negative E' are also set
227 to zero (Liu et al., 2021).

228



229 **Figure 2.** (a) The spatial distribution of original wind divergence ($\overline{D_d^W}$). (b) Elevation
 230 map generated from the GMTED2010 data set at 30 arcsecs
 231 (http://topotools.cr.usgs.gov/GMTED_viewer/). (c) Divergence of the background ($\overline{D_d^B}$)
 232 calculated with original daily wind field in 2019. (d) Divergence of methane
 233 enhancement ($\overline{D_d^B}$) under 500 meters with original daily wind field. (e)-(f) are similar
 234 to (c)-(d) but with the daily non-divergent wind field (U and V). The green “+” in (f) is
 235 used to generate the time series of D_d^B and D_d^S in Figure 5b.

236

237 2.4 Build temporal filter to identify possible false sources

238 The artifacts caused by the variability of spectral albedo (e.g., specific soil types and
 239 interferences in the spectral range of the retrieval windows) have been generally
 240 reduced in the WFMD v18 product (Schneising et al., 2023). The unrealistic



241 enhancements are reduced/removed over most locations. However, the biases
242 mentioned above can still exist in some places, as shown in Figure 3. In the northeast
243 near Riyadh, the stripe-shaped XCH₄ enhancements (Fig. 3a) coincide with the
244 locations of high albedos (Fig. 3b) that cannot be explained by the changes of elevations
245 from southwest to northeast (Fig. 3c). The relevant correction has been done by
246 machine learning calibration in the WFMD v18 product, thus we found no universal
247 pattern that can be used to describe the relationship among XCH₄, surface albedo and
248 aerosol. Therefore, we do not correct this kind of bias, following Liu et al. (2021), to
249 avoid double-correction. Alternatively, we try to find an objective way to filter false
250 emissions caused by retrieval artifacts.

251 A grid cell with a large E' but no significant linear correlation between $\overline{D_a^S}$ and $\overline{D_a^B}$
252 contains either a source or caused by artifacts in the retrieval, such as the case shown
253 in Fig. 3. If the enhancement is a kind of artifact; for example, caused by a bright surface,
254 it behaves more like a constant over days. Therefore, temporal variations of D_a^S will be
255 mainly dominated by daily variations of the background, according to Eq (1).
256 Considering that the values of D_a^B are much higher than D_a^S , as XCH_4^{PBL} is used to
257 calculate D_a^B while $(XCH_4^{PBL} - XCH_4^S)$ is used to calculate D_a^S , we normalize time
258 series of D_a^S and D_a^B , respectively. This normalization allows for a better comparison of
259 their temporal variations (amplitudes). The temporal filter is based on their normalized
260 time series and built as follows. Firstly, we remove the grid cells that have less than 10-
261 day records. Next, if more than half of the days in the time series of a grid cell have a
262 normalized positive D_a^S larger than D_a^B , the derived source (grid cell) is considered to
263 have high confidence level. As an example, we take a grid cell (showing with a green
264 “+” in Fig. 3e) that is affected by the albedo near Riyadh. It has a larger $\overline{D_a^S}$ than its
265 surrounding grid cells, but the linear regression is not applicable here (p_value of Eq.
266 (3) is 0.2), suggesting the regional background we built is not biased. However, only
267 20% (value of R in Fig. 4) of the total reliable days in 2019 have larger positive
268 normalized D_a^S (Fig. 4b), indicating the daily variation is not significantly different
269 from its background. Hence the reliability of this source needs to be checked. In contrast,
270 more than 50% of the total days of the grid cell, which is verified as a true source in
271 Tehran (a green “+” in Fig. 3e), have larger positive normalized D_a^S . In this way, the
272 emissions from an artifact or random noise from the retrieval can be objectively
273 identified. In this study, we set the temporal filter such that at least more than 50%
274 observations from the time series have a larger positive normalized D_a^S than the
275 normalized D_a^B .

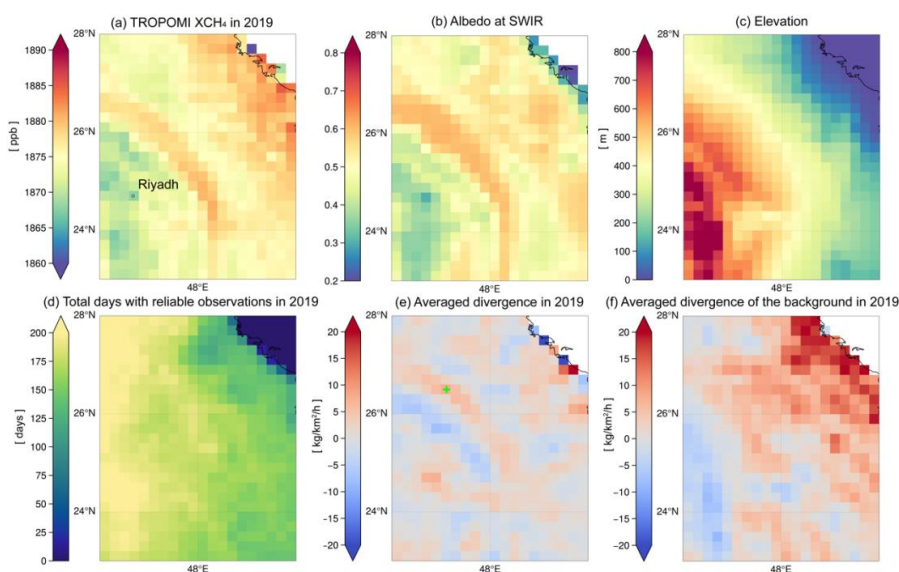
276 However, we should also be aware that the threshold of the temporal filter used in this
277 study is relatively rigid, possibly excluding sources that occasionally release a large
278 amount of methane, like intermittent oil/gas leakage and inappropriately burned waste
279 gases. The preserved sources that pass the temporal filter are suggested to be more



280 constant. For grid cells not affected by retrieval issues, the role of the temporal filter is
 281 more like an indication of the persistence or regional significance of a source, and the
 282 emissions without the temporal filter might, in some cases, be more realistic. The role
 283 of the temporal filter will be further discussed in Sect. 3

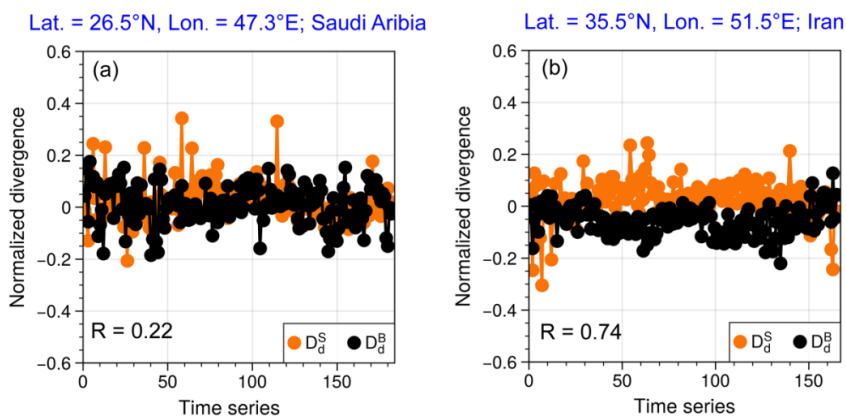
284 In addition, we use a Monte Carlo experiment to assess the uncertainty of the emissions.
 285 We randomly select 80% of the time series of D_d^S of a grid cell and calculated emissions
 286 based on this subset. The one standard deviation of those subsets will be used as an
 287 estimation of the uncertainty of the emission of this grid cell. The details of building
 288 the temporal filter and calculating the uncertainties are explained in SI part C.

289



290 **Figure 3.** Gridded $0.2^\circ \times 0.2^\circ$ annual average of (a) TROPOMI observed XCH₄ and
 291 corresponding (b) TROPOMI apparent albedo at the short-wave infrared wavelength
 292 (SWIR). (c) The gridded elevation map that is generated from the GMTED2010 data
 293 set at 30 arcsec (http://topotools.cr.usgs.gov/GMTED_viewer/). (d) The total number
 294 of valid observation days in 2019. (e) Averaged daily divergence ($\overline{D_d^S}$) and (f)
 295 divergence of the background ($\overline{D_d^B}$) in 2019. The green “+” in (e) is used to generate
 296 the time series of D_d^B and D_d^S in Figure 4(a).

297



298 **Figure 4.** The time series of normalized D_d^S (orange line) and D_d^B (black line) of the
 299 grid cell in (a) Saudi Arabia and (b) Iran. The “R” in the lower left corner stands for the
 300 ratio of the number of days with a larger positive normalized $\overline{D_d^S}$ than $\overline{D_d^B}$ related to the
 301 total number of sampled days.

302

303 **3 Results**

304 *3.1 Deriving the final emissions with the temporal filter*

305 After we derived emissions based on the divergence, the possible false sources are
 306 further identified by the temporal filter. The strict temporal filter is introduced to
 307 objectively exclude artifacts related to retrieval issues. However, to a grid cell that is
 308 not affected by retrieval issues, the temporal filter acts more like an indication of the
 309 persistence of a source. Namely, methane is intermittently released from this source.
 310 Here we selected two areas in the Middle East to illustrate the role of the temporal filter
 311 in the emission estimation. Our methane annual emissions are then compared with three
 312 widely-used methane emission inventories in the same year, 2019. Other auxiliary
 313 datasets such as NO_x emission inventories, methane plume complexes detected by
 314 EMIT imaging spectrometer and heating sources identified by VIIRS are also used to
 315 better evaluate our derived emissions.

316 Figure 5a and c show all possible sources and their relative uncertainties, respectively.
 317 Fig. 5b shows the final emissions after excluding the grid cells with emissions less than
 318 3 kg/km²/h, which is used as detection threshold of a source in this study. It is estimated
 319 by using the detection threshold of TROPOMI XCH₄ (Hu et al., 2018). The detection
 320 threshold of methane source from TROPOMI is depending on many factors such as
 321 source types, inversion methods and temporal coverage over a location etc., which can



322 vary from ~ 0.5 kg/km²/h to 12.5 kg/km²/h (Lauvaux et al., 2022; Dubey et al., 2023;
323 Jacob et al., 2016; 2022). Fig. 5a suggests presence of small sources around the center
324 of Riyadh, where a number of heating sources are detected by VIIRS. Additionally,
325 small sources are detected in the south to Riyadh, where dairy farms and industry areas
326 are located. The spatial distributions over two areas are similar to the DECSO NO_x
327 emissions, indicating existence of human activities. However, we found sources below
328 the detection threshold show large uncertainties (>20%) in this study, which means the
329 method is not robust to distinguish these small sources from the regional background.

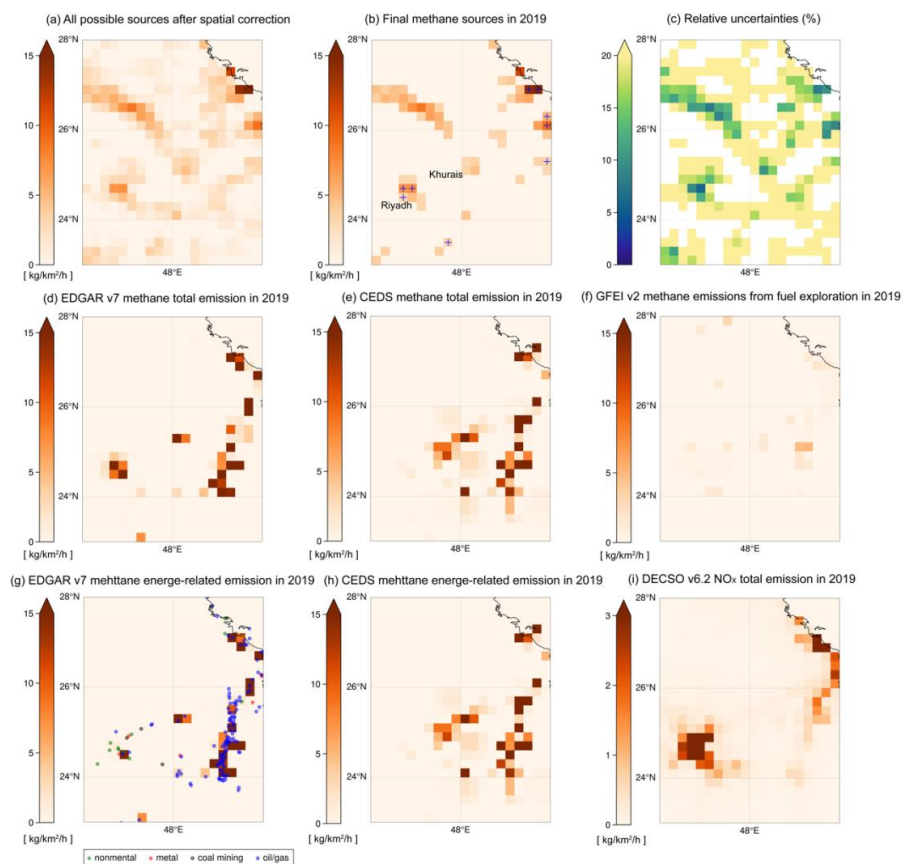
330 Both constant sources and artifacts (the “stripe” in the north of Riyadh) show small
331 relative uncertainties (Fig.5c) due to continuous regional enhancement of XCH₄. Only
332 a few sources pass the temporal filter in the middle of Saudi Arabia (marked by blue
333 “+” in Fig. 5b, indicating they are with high confidence). However, some facilities are
334 found over the Khurais oil field in Google Earth image while it fails to pass the temporal,
335 indicating they might be true but not constant. Another similar case is in the middle of
336 the Syria Arab Republic, where many methane plumes along the Euphrates River are
337 detected by the EMIT instrument (Fig. 6b) but reported quite low by three bottom-up
338 emission inventories. They are reported as non-continuous sources (fail to pass the
339 temporal filter) in our emission inventory (Fig. 6a). Thus, applying the strict temporal
340 filter in an area without retrieval issues is aim to identify continuous sources. In addition,
341 except for the capital, Riyadh, both EDGAR and CEDS show that the primary type of
342 sources in Saudi Arabia is energy related. The locations of oil/gas-related fires also
343 match well with the sources of methane in the eastern area in Fig. 5g. However, our
344 estimates (Fig. 5b) and methane emissions from the fuel exploitation reported by GFEI
345 v2 (Fig. 5f) are quite low (lower than the TROPOMI detection threshold) in the eastern
346 oil/gas production area. This finding is similar to the result of Lauvaux et al. (2022) that
347 fewer ultra-emitters of methane are detected by using the TROPOMI CH₄ operational
348 product (Lorente et al., 2021) in Middle Eastern countries such as Kuwait and Saudi
349 Arabia, which could be attributed to fewer accidental releases and/or stringent
350 maintenance operations. Using the locations and frequency of flares to estimate the
351 methane emission in bottom-up emission inventories could have led to overestimation
352 of the methane emissions in this region.

353 In contrast, Figure 7 show the case over Tehran and its surroundings. Most sources in
354 this area pass the strict temporal filter, indicating they are quite constant. Five areas are
355 identified as hotspots of methane sources in Fig. 7b. Fig. 7d-f shows the spatial
356 distributions of methane sources estimated by EDGAR, CEDS and GFEI in 2019. The
357 bottom-up emission inventories show lower methane emissions than our results. The
358 dominant category of methane sources in this area is not energy-related but others like
359 waste treatment and agriculture (see classification in Table-1), as suggested by EDGAR
360 and CEDS. A number of heat sources due to mental or non-mental industry production
361 are also identified by VIIRS over these hotspots. A good match in locations between
362 methane and NO_x sources over Tehran, Isfahan, and Atarabad is found when we further

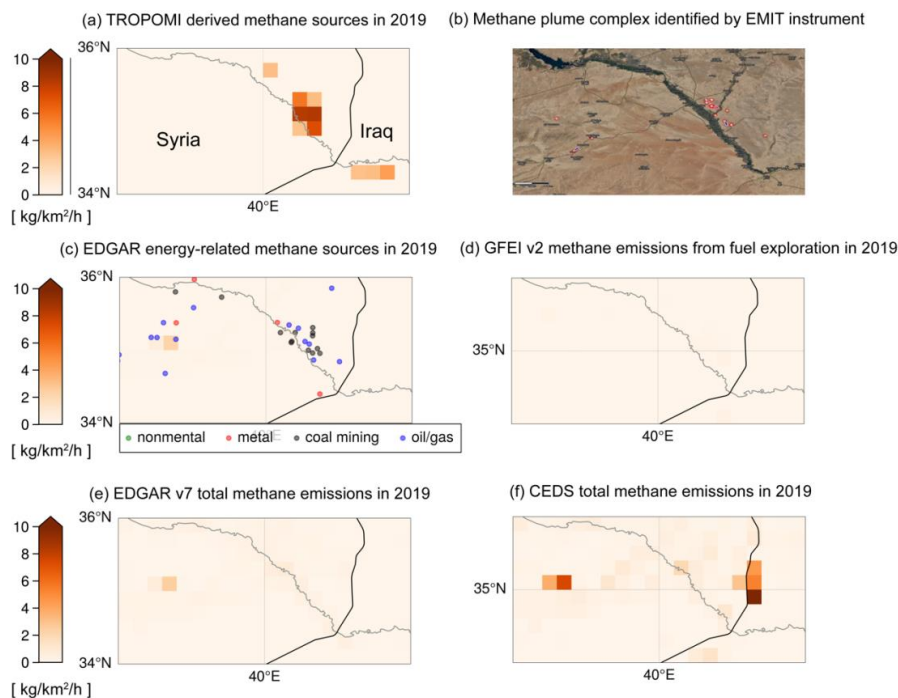


363 examine NO_x source distributions in EDGAR and DECSO. One possible reason for the
364 consistence over these areas can be that the methane emissions may come from waste
365 treatment in cities, where landfilling is the most common way of municipal solid waste
366 (MSW) disposal in Iran (Pazoki et al., 2015). Fig. 7c presents a case of methane plume
367 identified by EMIT instrument on 23th April 2023 near Kashan power plant that is
368 apparently not reported in current inventories. Actually, some facilities have been found
369 in Google Earth images near Kashan, which are also identified by our method in Fig.
370 7b. Another hotspot area located between Tehran and Kashan is the area near Kavir
371 National Park, where we currently have no clear explanations about emissions.

372



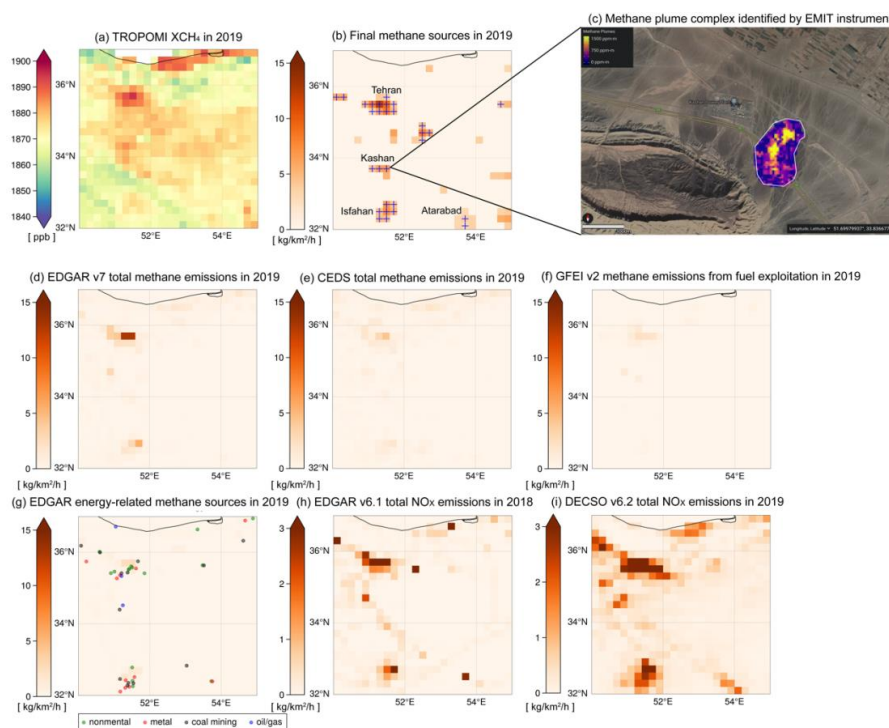
373 **Figure 5.** (a) Averaged annual methane total emissions derived from the divergence
 374 after the spatial correction in the middle of Saudi Arabia. (b) All possible sources above
 375 the TROPOMI detection threshold ($3\text{kg}/\text{km}^2/\text{h}$). Grid cells that pass the temporal filter
 376 are marked by blue “+”. (c) The relative uncertainty of derived methane emissions in
 377 (a). (d) EDGAR v7.0 averaged annual methane total emission in 2019. (e) CEDS
 378 v_2021_04_21 averaged annual total methane emissions in 2019. (f) GEFI v2 averaged
 379 annual methane emissions from fuel exploration in 2019. (g) Energy-related methane
 380 emissions from EDGAR v7.0 overlapped with the industrial heat sources identified by
 381 VIIRS instrument. (h) CEDS v_2021_04_21 energy-related methane emissions in 2019.
 382 (i) Averaged annual DECISO v6.2 NO_x total emission in 2019. The spatial resolution of
 383 all emission data showing here is $0.2^\circ \times 0.2^\circ$.



384 **Figure 6.** (a) Averaged annual methane emissions over Syria from TROPOMI
 385 observation in 2019. (b) The detected methane plume complex (red circles) by EMIT
 386 instrument. (Note: EMIT was launched in 2020 and methane plumes are recorded since
 387 10th August 2022; Source: [https://earth.jpl.nasa.gov/emit/data/data-portal/Greenhouse-](https://earth.jpl.nasa.gov/emit/data/data-portal/Greenhouse-Gases/)
 388 [Gases/](https://earth.jpl.nasa.gov/emit/data/data-portal/Greenhouse-Gases/)) (c) Energy-related methane emissions from EDGAR v7.0 overlapped with the
 389 industrial heat sources identified by VIIRS instrument. (d) GFEI v2 methane emissions
 390 from the fuel exploitation in 2019. (e) EDGAR v7.0 emission inventory in 2019. (f)
 391 CEDS v_2021_04_21 total methane emissions in 2019. The spatial resolution of all
 392 emission data showing here is $0.2^\circ \times 0.2^\circ$.



393



394 **Figure 7.** (a) The spatial distribution of TROPOMI observed XCH₄ in 2019 on a grid
 395 of 0.2°. (b) The methane sources derived from TROPOMI after the spatial correction
 396 and are higher than 3kg/km²/h (inferred from the detection threshold of TROPOMI
 397 XCH₄). The grid cells with high confidence, passing the temporal filter, are marked by
 398 a blue “+”. (c) The detected methane plume complex by EMIT instrument in Kashan
 399 on 23th April 2023 (Source: <https://earth.jpl.nasa.gov/emit-mmgis-lb/?s=e7z1z>). EMIT
 400 was launched in 2020 and methane plumes are recorded since 10th August 2022. (d)
 401 EDGAR v7.0 averaged annual methane total emission in 2019. (e) CEDS
 402 v_2021_04_21 averaged annual total methane emissions in 2019. (f) GFEI v2 averaged
 403 annual methane emissions from the fuel exploitation in 2019. (g) Energy-related
 404 methane emissions from EDGAR v7.0 overlapped with the industrial heat sources
 405 identified by VIIRS instrument. (h) Averaged annual EDGAR v6.1 NO_x total emission
 406 in 2019. (i) Averaged annual DECSO v6.2 NO_x total emission in 2019.

407 *3.2 Annual CH₄ emissions over the Middle East based on TROPOMI*

408 In Figure 8, we select five hotspot regions in the Middle East hardly influenced by
 409 retrieval issues to further assess the annual regional emissions. Therefore, the results of
 410 all possible sources (pink bars) may be more representative of the total emissions in
 411 these areas, and the emissions passing the temporal filters (blue bars) can be used to



412 estimate the contribution of constant sources. The areas used to calculate annual
413 emissions (bars in Fig. 8) are shown as dark green rectangles in the insets on the top.
414 The emission map in each panel of Fig. 8 is the annual methane emissions of EDGAR
415 v7.0 in 2019. The energy-related sectors and the other categories (waste, agriculture,
416 and transportation) of EDGAR v7.0 methane emissions from 2018 to 2021 are
417 displayed by the first stacked green/yellow bars in Fig. 8a–e. The category-based annual
418 emissions of CEDS in 2018 and 2019 are shown in the last stacked purple/orange bars.
419 The estimate of GFEI for the fuel exploration in 2019 is shown as a red asterisk
420 overlapped on the third column. We should clarify that our estimate for the total
421 emission in each year is the sum of sources that are higher than 3kg/km²/h in the study
422 area, but the total emission reported by a bottom-up emission inventory includes grid
423 cells with emissions across all ranges. Thus, theoretically our estimates will
424 underestimate the real emissions.

425 The main type of methane sources in Tehran and Isfahan given by EDGAR and CEDS
426 is waste, and the energy-related sources are not oil/gas production based on VIIRS
427 detected fire types and EDGAR's prediction (Fig. 7g). The derived methane emissions
428 are also more constant. Smaller differences are found between the blue and pink bars
429 than Riyadh, West of Turkmenistan and Iran & Iraq (Fig. 8c-e). Our estimates in Tehran
430 are 12-30% higher and 33-52% higher than EDGAR's and CEDS's estimates for
431 constant sources, respectively. GFEI's estimate for the fuel exploration is 2-3 times
432 higher than EDGAR's and CEDS's estimates, indicating possible underestimations of
433 the two inventories in Tehran. The sources in Isfahan, another Iranian metropolis, are
434 also constant over time (very small difference between blue and pink bars). However,
435 our derived emissions are about 3 times higher than the two inventories. Sources in our
436 inventory are distributed over a wider area in Isfahan, and their spatial distributions are
437 similar to NO_x sources of EDGAR and DECSO, indicating the emissions are very
438 likely from activities in the city. Although Isfahan has been attempting to gradually
439 transform the landfill-based disposal system into a modern system with less production
440 of greenhouse gases, the high methane emissions we derived might also imply that
441 waste management is still a challenge (Abdoli et al., 2016). A similar result was found
442 by Chen et al. (2023), in which they found waste emissions could be underestimated by
443 more than 50% in certain Middle Eastern countries like Iran, Iraq, and Saudi Arabia.

444 The total constant emissions we derived for Riyadh are half that of EDGAR but close
445 to CEDS's estimate. As shown in Fig. 5, the spatial distributions of various inventories
446 can be very different. The domain we used to calculate the total emission is defined by
447 the spatial distribution of EDGAR, but oil/gas-related flares are located in the northeast
448 of Riyadh (blue dots in Fig. 5g). However, including these cells only increases total
449 emissions by 5–8% because they are smaller than 3/kg/km² therefore below the
450 detection threshold of TROPOMI. Moreover, ~50% of the emissions in Riyadh are
451 constant (have constant emission factor), which can be another reason of the large
452 discrepancy between different inventories.

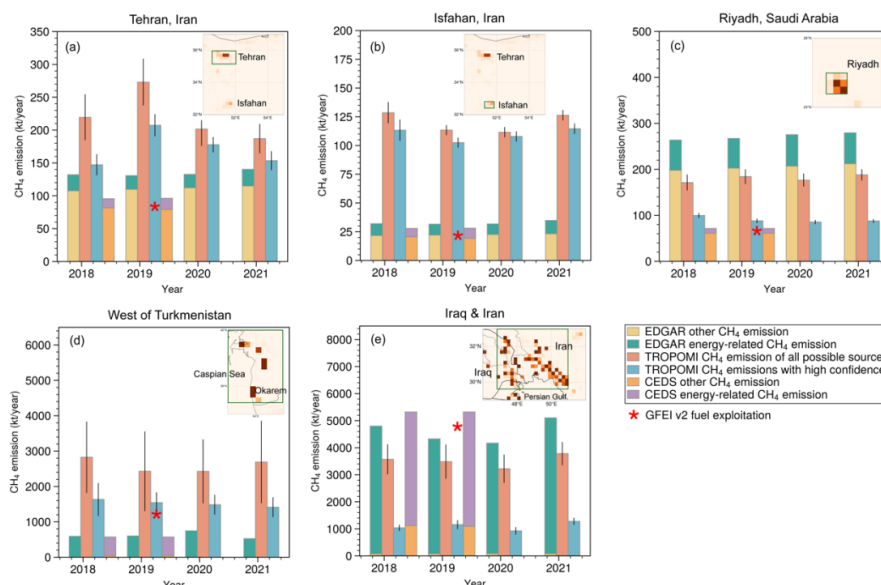


453 Western Turkmenistan near the Caspian Sea and the coastal regions of Iran and Iraq are
454 two well-known oil/gas production areas in the Middle East. The energy-related sectors
455 (green bars) contribute more than 92% in the two regions based on EDGAR estimates.
456 The constant emissions derived from TROPOMI (blue bars) in the west of
457 Turkmenistan are quite comparable to GFEL's estimate but nearly two times higher than
458 estimates of EDGAR and CEDS. Although total methane emissions estimated by
459 EDGAR and CEDS are very similar, the spatial distributions of sources are different
460 (Figure S1). The constant sources of oil/gas there contribute to ~55% of the total
461 emissions over the four years based on our estimates, which agrees with Varon et al.
462 (2021), who concluded the sources here are intermittent, and the persistence rate is
463 ~40%. Our estimates will be four times higher than the total emissions of these two
464 inventories if all possible sources are included. The large uncertainty also implies that
465 resolving the sources here can be quite difficult because of the few observations near
466 the coast and the variabilities of the sources.

467 The annual variations in the coastal area of Iraq and Iran are consistent in EDGAR's
468 and our estimates (the offshore emissions in bottom-up emission inventories are
469 ignored because the observation of TROPOMI over ocean can be quite difficult). It
470 increased to surpass the total emission of 2018 in 2021 after a modest decline from
471 2018 to 2020. The fraction of constant sources is much less than in Western
472 Turkmenistan. Our estimates are comparable to EDGAR if all possible sources are
473 included. However, the total emissions from constant sources are quite low, and they
474 are comparable to the other methane emissions estimated by CEDS, which mainly come
475 from waste and are quite low in EDGAR estimates. Chen et al. (2023) found that oil/gas
476 emission derived from their inverse modeling with the TROPOMI observation is 43%
477 and 58% lower than in their bottom-up emission inventory over Iran and Iraq,
478 respectively. Lauvaux et al. (2022) also showed fewer ultra-emitters of methane are
479 detected by using the TROPOMI CH₄ operational product (Lorente et al., 2021) in
480 Middle Eastern countries such as Kuwait and Saudi Arabia, which could be attributed
481 to fewer accidental releases and/or stringent maintenance operations. Thus, for an area
482 with many occasionally released methane, using a constant emission factor or flaring
483 data as an index may lead to an overestimation of methane leakage from the oil/gas
484 industry. In addition, we checked plume complexes detected by EMIT, and find that the
485 max value of each plume complex can differ by an order of magnitude, implying the
486 large variabilities of released methane here. The coarse spatial resolution of our
487 emission data may smooth plume complexes and can be another reason of predicted
488 lower emissions.



489



490 **Figure 8.** Regional total methane annual emissions estimated by EDGAR v7.0 and
 491 TROPOMI from 2018 to 2021. The areas used to generate bars in (a–e) are shown in
 492 dark green rectangles in embraced emission maps of total emissions of EDGAR in 2019.
 493 The ranges in latitudes and longitudes can be found in Table S1 in SI. A green bar
 494 represents the energy-related emissions, and a yellow bar represents the remaining
 495 methane emissions in EDGAR v7.0. A purple bar represents the energy-related
 496 emissions, and an orange bar represents the remaining methane emissions in CEDS
 497 v_2021_04_21. The blue bar is the total emission of sources that pass the temporal filter
 498 and are higher than 3kg/km²/h. The pink bar represents the total emission of all possible
 499 sources that are higher than 3kg/km²/h. All the emissions over water (the Caspian Sea
 500 and the Persian Gulf) are ignored because of too few observations and large
 501 uncertainties. An error bar represents the sum of uncertainties associated with each
 502 source in this area. The calculation of the uncertainty of a source (grid cell) is presented
 503 in Sect. 2.4 and the SI Part C.

504

505 4 Conclusions

506 An improved divergence method using non-divergent wind fields with the temporal
 507 filter has been developed to better estimate CH₄ emissions from observations of the
 508 TROPOMI instrument over areas with complicated orography and/or high albedo, like
 509 the Middle East. The non-divergent wind largely reduces the biases caused by drastic
 510 topography changes. The residue of the background (e.g., sources in Tehran, located in
 511 a valley) is further subtracted from the emission through spatial correction. The



512 temporal filter is built to further exclude false sources due to retrieval issues. It also can
513 be used to test the persistency of sources over an area free of artifacts. We found that
514 emissions from wastes (e.g., landfills, wastewater) or agriculture (e.g., livestock farms)
515 can be quite persistent in time compared to the oil/gas-related sources in the Middle
516 East.

517 We further compared our annual regional total emissions with EDGAR v7.0, CEDS
518 v2021_04_21 and GFEI v2 for various regions in the Middle East with different source
519 categories from 2018 to 2021. The oil/gas productions at the coast of Iran and Iraq are
520 quite intermittent compared to the west of Turkmenistan where our estimate for
521 constant sources is quite comparable to the emission from the fuel exploitation
522 estimated by GFEI v2. The continuous release of methane from waste or farms can
523 contribute considerably to the total methane emissions in several metropolises in the
524 Middle East, which can be two times higher than EDGAR's and CEDS's estimates.

525 In future work, the role of the temporal filter can be largely reduced with new improved
526 retrieval products of TROPOMI CH₄. This will especially allow better estimates of
527 intermittent methane emissions.

528 *Acknowledgments*

529 *Competing interests.*

530 The authors declare that they have no competing interests.

531 *Funding.*

532 ESA project IMPALA, grant number: 4000139771/22/I-DT-bgh

533 *Author contributions.*

534 ML, RVA, and MVW designed the experiment and analyze the results. ML performed
535 all calculations and visualized the results. The codes for estimating methane emissions
536 are mainly developed by ML and are supported by LB, HE and PV. HK and JD help to
537 visualize the results. The wind fields are extracted by HE. YL provides the category-
538 related VIIRS data. All co-authors contributed to review the manuscript.



539 **Data and materials availability:**

540 TROPOMI/WFMD v1.8 methane Level-2 dataset is available at: [https://www.iup.uni-](https://www.iup.uni-bremen.de/carbon_ghg/products/tropomi_wfmd/)
541 [bremen.de/carbon_ghg/products/tropomi_wfmd/](https://www.iup.uni-bremen.de/carbon_ghg/products/tropomi_wfmd/)

542 EAC4 of CAMS, which used to be estimated the column above the PBL can be accessed
543 at: [https://ads.atmosphere.copernicus.eu/cdsapp#!/dataset/cams-global-reanalysis-](https://ads.atmosphere.copernicus.eu/cdsapp#!/dataset/cams-global-reanalysis-eac4?tab=overview)
544 [eac4?tab=overview](https://ads.atmosphere.copernicus.eu/cdsapp#!/dataset/cams-global-reanalysis-eac4?tab=overview)

545 EDGAR v7.0 for methane anthropogenic emissions and EDGAR v6.1 for NO_x
546 anthropogenic emissions are available at:
547 https://edgar.jrc.ec.europa.eu/overview.php?v=432_GHG

548 CEDS v_2021_04_21 for methane anthropogenic emissions is available at:
549 <https://data.pnnl.gov/dataset/CEDS-4-21-21>

550 GFEI v2 for the methane emissions from fuel exploitation is available at:
551 [https://dataverse.harvard.edu/dataset.xhtml?persistentId=doi:10.7910/DVN/HH4EUM](https://dataverse.harvard.edu/dataset.xhtml?persistentId=doi:10.7910/DVN/HH4EUM&version=2.0)
552 [&version=2.0](https://dataverse.harvard.edu/dataset.xhtml?persistentId=doi:10.7910/DVN/HH4EUM&version=2.0)

553 MODIS daily 10km AOD data can be downloaded through NASA Earthdata portal:
554 <https://search.earthdata.nasa.gov/search>

555 DECSO total anthropogenic NO_x emission is available at: www.globemission.eu

556 The CH₄ plume complexes detected by EMIT instrument are available at:
557 <https://earth.jpl.nasa.gov/emit/data/data-portal/Greenhouse-Gases/>

558 **Reference**

559 Abdoli, M., Rezaei, M., & Hasanian, H., 2016. Integrated solid waste management in
560 megacities. *Global Journal of Environmental Science and Management*, 2(3), 289-298.
561 doi: 10.7508/gjesm.2016.03.008

562 Beirle, S., C. Borger, S. Dörner, A. Li, Z. Hu, F. Liu, Y. Wang, and T. Wagner (2019),
563 Pinpointing nitrogen oxide emissions from space, *Science Advances*, 5(11), eaax9800.

564 Chen, Z., Jacob, D. J., Gautam, R., Omara, M., Stavins, R. N., Stowe, R. C., Nesser, H.,
565 Sulprizio, M. P., Lorente, A., Varon, D. J., Lu, X., Shen, L., Qu, Z., Pendergrass, D. C.,
566 and Hancock, S.: Satellite quantification of methane emissions and oil–gas methane
567 intensities from individual countries in the Middle East and North Africa: implications
568 for climate action, *Atmos. Chem. Phys.*, 23, 5945–5967, [https://doi.org/10.5194/acp-](https://doi.org/10.5194/acp-23-5945-2023)
569 [23-5945-2023](https://doi.org/10.5194/acp-23-5945-2023), 2023.



- 570 Crippa, M., Guizzardi, D., Banja, M., Solazzo, E., Muntean, M., Schaaf, E., Pagani, F.,
571 Monforti-Ferrario, F., Olivier, J., Quadrelli, R., Risquez Martin, A., Taghavi-Moharamli,
572 P., Grassi, G., Rossi, S., Jacome Felix Oom, D., Branco, A., San-Miguel-Ayanz, J. and
573 Vignati, E., CO₂ emissions of all world countries – JRC/IEA/PBL 2022 Report, EUR
574 31182 EN, Publications Office of the European Union, Luxembourg,
575 2022, [doi:10.2760/730164](https://doi.org/10.2760/730164), JRC130363.
- 576 de Gouw, J.A., Veefkind, J.P., Roosenbrand, E., Dix, B., Lin, J.C., Landgraf, J., Levelt,
577 P.F., 2020. Daily Satellite Observations of Methane from Oil and Gas Production
578 Regions in the United States. *Scientific Reports* 10(1), 1379.
579 <https://doi.org/10.1038/s41598-020-57678-4>.
- 580 Ding, J., van der A, R. J., Eskes, H. J., Mijling, B., Stavrakou, T., van Geffen, J. H.
581 G. M., Levelt, P. F., 2020. NO_x emissions reduction and rebound in China due to the
582 COVID-19 crisis. *Geophysical Research Letters*, 46,
583 e2020GL089912. <https://doi.org/10.1029/2020GL089912>
- 584 Dlugokencky, E.J., Bruhwiler, L., White, J.W.C., Emmons, L.K., Novelli, P.C.,
585 Montzka, S.A., Masarie, K.A., Lang, P.M., Crotwell, A.M., Miller, J.B., Gatti, L.V.,
586 2009. Observational constraints on recent increases in the atmospheric CH₄ burden.
587 *Geophysical Research Letters* 36(18).
588 <https://doi.org/https://doi.org/10.1029/2009GL039780>.
- 589 Dubey L, Cooper J, Hawkes A. Minimum detection limits of the TROPOMI satellite
590 sensor across North America and their implications for measuring oil and gas methane
591 emissions. *Sci Total Environ.* 2023 May 10;872:162222. doi:
592 10.1016/j.scitotenv.2023.162222. Epub 2023 Feb 14. PMID: 36796684.
- 593 Eyring, V., N.P. Gillett, K.M. Achuta Rao, R. Barimalala, M. Barreiro Parrillo, N.
594 Bellouin, C. Cassou, P.J. Durack, Y. Kosaka, S. McGregor, S. Min, O. Morgenstern,
595 and Y. Sun, 2021: Human Influence on the Climate System. In *Climate Change 2021:
596 The Physical Science Basis. Contribution of Working Group I to the Sixth Assessment
597 Report of the Intergovernmental Panel on Climate Change*[Masson-Delmotte, V., P.
598 Zhai, A. Pirani, S.L. Connors, C. Péan, S. Berger, N. Caud, Y. Chen, L. Goldfarb, M.I.
599 Gomis, M. Huang, K. Leitzell, E. Lonnoy, J.B.R. Matthews, T.K. Maycock, T.
600 Waterfield, O. Yelekçi, R. Yu, and B. Zhou (eds.)]. Cambridge University Press,
601 Cambridge, United Kingdom and New York, NY, USA, pp. 423–552,
602 doi:10.1017/9781009157896.005.
- 603 Food and Agriculture Organization of the United Nations (FAO).
604 <https://www.fao.org/home/en/>
- 605 Guo, J., Zhang, J., Yang, K., Liao, H., Zhang, S., Huang, K., Lv, Y., Shao, J., Yu, T.,
606 Tong, B., Li, J., Su, T., Yim, S. H. L., Stoffelen, A., Zhai, P., and Xu, X.: Investigation



- 607 of near-global daytime boundary layer height using high-resolution radiosondes: first
608 results and comparison with ERA5, MERRA-2, JRA-55, and NCEP-2 reanalyses,
609 *Atmos. Chem. Phys.*, 21, 17079–17097, <https://doi.org/10.5194/acp-21-17079-2021>,
610 2021.
- 611 Inness, A., Ades, M., Agustí-Panareda, A., Barré, J., Benedictow, A., Blechschmidt,
612 A.M., Dominguez, J.J., Engelen, R., Eskes, H., Flemming, J., Huijnen, V., Jones, L.,
613 Kipling, Z., Massart, S., Parrington, M., Peuch, V.H., Razinger, M., Remy, S., Schulz,
614 M., Suttie, M., 2019. The CAMS reanalysis of atmospheric composition. *Atmos. Chem.*
615 *Phys.* 19(6), 3515-3556. <https://doi.org/10.5194/acp-19-3515-2019>.
- 616 International Energy Agency (IEA) data and statistics (2021). [https://www.iea.org/data-](https://www.iea.org/data-and-statistics)
617 [and-statistics](https://www.iea.org/data-and-statistics).
- 618 Jacob, D. J., Turner, A. J., Maasakkers, J. D., Sheng, J., Sun, K., Liu, X., et al. (2016).
619 Satellite observations of atmospheric methane and their value for quantifying methane
620 emissions. *Atmos. Chem. Phys.*, 16(22), 14371-14396. doi:10.5194/acp-16-14371-2016
- 621 Jacob, D. J., Varon, D. J., Cusworth, D. H., Dennison, P. E., Frankenberg, C., Gautam,
622 R., et al. (2022). Quantifying methane emissions from the global scale down to point
623 sources using satellite observations of atmospheric methane. *Atmospheric Chemistry*
624 *and Physics*, 22(14), 9617-9646. doi:10.5194/acp-22-9617-2022
- 625 K. Sims, Fluid flow tutorial, 2018. Available: [https:// www.karlsims.com/fluid-](https://www.karlsims.com/fluid-flow.html)
626 [flow.html](https://www.karlsims.com/fluid-flow.html).
- 627 Lauvaux, T., Giron, C., Mazzolini, M., d'Aspremont, A., Duren, R., Cusworth, D.,
628 Shindell, D., Ciais, P., 2022. Global assessment of oil and gas methane ultra-emitters.
629 *Science* 375(6580), 557-561. <https://doi.org/doi:10.1126/science.abj4351>.
- 630 Liu, M., van der A, R., van Weele, M., Eskes, H., Lu, X., Veeffkind, P., de Laat, J.,
631 Kong, H., Wang, J., Sun, J., Ding, J., Zhao, Y., Weng, H., 2021. A new divergence
632 method to quantify methane emissions using observations of Sentinel-5P
633 TROPOMI. *Geophysical Research Letters*, 48,
634 e2021GL094151. <https://doi.org/10.1029/2021GL094151>
- 635 Liu, Y., Hu, C., Zhan, W., Sun, C., Murch, B., Ma. L., 2018. Identifying industrial heat
636 sources using time-series of the VIIRS Nightfire product with an object-oriented
637 approach. *Remote Sens. Environ.*, 204, pp. 347-365.
638 <https://doi.org/10.1016/j.rse.2017.10.019>
- 639 Mijling, B., & van der A, R. J., 2012. Using daily satellite observations to estimate
640 emissions of short-lived air pollutants on a mesoscopic scale. *Journal of Geophysical*
641 *Research*, 117, D17302. <https://doi.org/10.1029/2012JD017817>



- 642
643 O'Rourke, Patrick, Smith, Steven J, Mott, Andrea R, Ahsan, Hamza, Mcduffie, Erin E,
644 Crippa, Monica, Klimont, Zbigniew, Mcdonald, Brian, Wang, Shuxiao, Nicholson,
645 Matthew B, Hoesly, Rachel M, and Feng, Leyang. *CEDS v_2021_04_21 Gridded*
646 *emissions data*. United States: N. p., 2021. Web.
647 doi:10.25584/PNNLDataHub/1779095.
- 648 Pandey, S., Gautam, R., Houweling, S., van der Gon, H.D., Sadavarte, P., Borsdorff, T.,
649 Hasekamp, O., Landgraf, J., Tol, P., van Kempen, T., Hoogeveen, R., van Hees, R.,
650 Hamburg, S.P., Maasackers, J.D., Aben, I., 2019. Satellite observations reveal extreme
651 methane leakage from a natural gas well blowout. *Proceedings of the National*
652 *Academy of Sciences* 116(52), 26376. <https://doi.org/10.1073/pnas.1908712116>.
- 653 Pazoki M, Maleki Delarestaghi R, Rezvanian M R, Ghasemzade R, Dalaei P. Gas
654 Production Potential in the Landfill of Tehran by Landfill Methane Outreach Program.
655 *Jundishapur J Health Sci*. 2015;7(4):e29679. <https://doi.org/10.17795/jjhs-29679>.
- 656 Rigby, M., Prinn, R.G., Fraser, P.J., Simmonds, P.G., Langenfelds, R.L., Huang, J.,
657 Cunnold, D.M., Steele, L.P., Krummel, P.B., Weiss, R.F., O'Doherty, S., Salameh, P.K.,
658 Wang, H.J., Harth, C.M., Mühle, J., Porter, L.W., 2008. Renewed growth of
659 atmospheric methane. *Geophysical Research Letters* 35(22).
660 <https://doi.org/https://doi.org/10.1029/2008GL036037>.
- 661 Saunio, M., Stavert, A. R., Poulter, B., Bousquet, P., Canadell, J. G., Jackson, R. B.,
662 Raymond, P. A., Dlugokencky, E. J., Houweling, S., Patra, P. K., Ciais, P., Arora, V. K.,
663 Bastviken, D., Bergamaschi, P., Blake, D. R., Brailsford, G., Bruhwiler, L., Carlson, K.
664 M., Carrol, M., Castaldi, S., Chandra, N., Crevoisier, C., Crill, P. M., Covey, K., Curry,
665 C. L., Etiope, G., Frankenberg, C., Gedney, N., Hegglin, M. I., Höglund-Isaksson, L.,
666 Hugelius, G., Ishizawa, M., Ito, A., Janssens-Maenhout, G., Jensen, K. M., Joos, F.,
667 Kleinen, T., Krummel, P. B., Langenfelds, R. L., Laruelle, G. G., Liu, L., Machida, T.,
668 Maksyutov, S., McDonald, K. C., McNorton, J., Miller, P. A., Melton, J. R., Morino, I.,
669 Müller, J., Murguía-Flores, F., Naik, V., Niwa, Y., Noce, S., O'Doherty, S., Parker, R. J.,
670 Peng, C., Peng, S., Peters, G. P., Prigent, C., Prinn, R., Ramonet, M., Regnier, P., Riley,
671 W. J., Rosentreter, J. A., Segers, A., Simpson, I. J., Shi, H., Smith, S. J., Steele, L. P.,
- 672 Thornton, B. F., Tian, H., Tohjima, Y., Tubiello, F. N., Tsuruta, A., Viovy, N.,
- 673 van der A, R. J., Ding, J., and Eskes, H.: Monitoring European anthropogenic NO_x
674 emissions from space, *EGUsphere* [preprint], [https://doi.org/10.5194/egusphere-2023-](https://doi.org/10.5194/egusphere-2023-3099)
675 [3099](https://doi.org/10.5194/egusphere-2023-3099), 2024
- 676 Voulgarakis, A., Weber, T. S., van Weele, M., van der Werf, G. R., Weiss, R. F., Worthly,
677 D., Wunch, D., Yin, Y., Yoshida, Y., Zhang, W., Zhang, Z., Zhao, Y., Zheng, B., Zhu,
678 Q., Zhu, Q., and Zhuang, Q.: The Global Methane Budget 2000–2017, *Earth Syst. Sci.*



- 679 Data, 12, 1561–1623, <https://doi.org/10.5194/essd-12-1561-2020>, 2020.
- 680 Scarpelli, T. R., Jacob, D. J., Grossman, S., Lu, X., Qu, Z., Sulprizio, M. P., Zhang, Y.,
681 Reuland, F., Gordon, D., and Worden, J. R.: Updated Global Fuel Exploitation
682 Inventory (GFEI) for methane emissions from the oil, gas, and coal sectors: evaluation
683 with inversions of atmospheric methane observations, *Atmos. Chem. Phys.*, 22, 3235–
684 3249, <https://doi.org/10.5194/acp-22-3235-2022>, 2022.
- 685 Schneider, A., Borsdorff, T., aan de Brugh, J., Aemisegger, F., Feist, D.G., Kivi, R.,
686 Hase, F., Schneider, M., Landgraf, J., 2020. First data set of H₂O/HDO columns from
687 the Tropospheric Monitoring Instrument (TROPOMI). *Atmos. Meas. Tech.* 13(1), 85–
688 100. <https://doi.org/10.5194/amt-13-85-2020>.
- 689
690 Schneising, O., Buchwitz, M., Hachmeister, J., Vanselow, S., Reuter, M., Buschmann,
691 M., Bovensmann, H., and Burrows, J. P.: Advances in retrieving XCH₄ and XCO from
692 Sentinel-5 Precursor: improvements in the scientific TROPOMI/WFMD algorithm,
693 *Atmos. Meas. Tech.*, 16, 669–694, <https://doi.org/10.5194/amt-16-669-2023>, 2023.
- 694 Turner, A.J., Frankenberg, C., Kort, E.A., 2019. Interpreting contemporary trends in
695 atmospheric methane. *Proceedings of the National Academy of Sciences* 116(8), 2805.
696 <https://doi.org/10.1073/pnas.1814297116>.
- 697 Varon, D. J., Jervis, D., McKeever, J., Spence, I., Gains, D., and Jacob, D. J.: High-
698 frequency monitoring of anomalous methane point sources with multispectral Sentinel-
699 2 satellite observations, *Atmos. Meas. Tech.*, 14, 2771–2785,
700 <https://doi.org/10.5194/amt-14-2771-2021>, 2021.
- 701 Veefkind, J.P., Aben, I., McMullan, K., Förster, H., de Vries, J., Otter, G., Claas, J.,
702 Eskes, H.J., de Haan, J.F., Kleipool, Q., van Weele, M., Hasekamp, O., Hoogeveen, R.,
703 Landgraf, J., Snel, R., Tol, P., Ingmann, P., Voors, R., Kruizinga, B., Vink, R., Visser,
704 H., Levelt, P.F., 2012. TROPOMI on the ESA Sentinel-5 Precursor: A GMES mission
705 for global observations of the atmospheric composition for climate, air quality and
706 ozone layer applications. *Remote Sensing of Environment* 120, 70–83.
707 <https://doi.org/https://doi.org/10.1016/j.rse.2011.09.027>.
- 708 Veefkind, J. P., Serrano-Calvo, R., de Gouw, J., Dix, B., Schneising, O., Buchwitz,
709 M., Barré, J., van der A, R.J., Liu, M., Levelt, P.F., 2023. Widespread frequent methane
710 emissions from the oil and gas industry in the Permian basin. *Journal of Geophysical*
711 *Research: Atmospheres*, 128,
712 e2022JD037479. <https://doi.org/10.1029/2022JD037479>
- 713 Zhang, Y., Gautam, R., Pandey, S., Omara, M., Maasackers, J.D., Sadavarte, P., Lyon,
714 D., Nesser, H., Sulprizio, M.P., Varon, D.J., Zhang, R., Houweling, S., Zavala-Araiza,
715 D., Alvarez, R.A., Lorente, A., Hamburg, S.P., Aben, I., Jacob, D.J., 2020. Quantifying

<https://doi.org/10.5194/egusphere-2024-370>

Preprint. Discussion started: 4 March 2024

© Author(s) 2024. CC BY 4.0 License.



716 methane emissions from the largest oil-producing basin in the United States from space.

717 Science Advances 6(17), eaaz5120. <https://doi.org/10.1126/sciadv.aaz5120>.

718